Comunicações Geológicas

Comunicações Geológicas (2024) 111, 1, 57-69
ISSN: 0873-948X; **e-ISSN:** 1647-581X

Reappraisal of active tectonics of the Porto Alto buried fault zone (Portugal) considering new geophysical shallow studies

Reavaliação da tectónica activa da zona de falha oculta de Porto Alto (Portugal) considerando novos estudos geofísicos superficiais

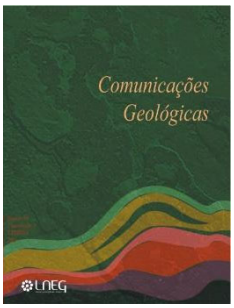

J. Carvalho[1*], J. Cabral[2], R. Ghose[3], J. Borges[4], R. Dias[1]

DOI: https://doi.org/10.34637/531q-s210
Recebido em 09/05/2024 / Aceite em 12/03/2025
Publicado online em maio de 2025

Artigo original
Original article

Abstract: The Lower Tagus Valley area (LTV), where Lisbon is located, has been affected by several destructive, M 6+ earthquakes whose sources remain to be determined. The identification of expectable surface or near surface ruptures in the area is a challenging task that requires a multidisciplinary analysis that includes geophysical techniques, as the source faults are mainly buried despite likely to deform Upper Pleistocene to Holocene alluvial cover of the Tagus River. This paper focuses on the characterization of the Porto Alto fault zone for seismic hazard mitigation purposes. The Porto Alto fault zone was recognized in oil-industry P-wave 1980's seismic reflection data as an important, Miocene reactivated, deep structure in the LTV. High-resolution P-wave seismic reflection data were later acquired in the early 2000's to investigate related Holocene fault activity, leading to the identification of a shallow fault zone near the surface. However, the vertical resolution of the acquired P-wave seismic reflection data was considered insufficient to corroborate any presumably small vertical offset related to fault rupture in the ca. 50 m thick alluvium cover. Trenching for the recognition and characterization of surface faulting was previously tested in the study region but it proved to be a challenging and poorly efficient methodology due to the very shallow water table (at ~1 m) and low cohesion of the sediments. Due to these constraints, we revisited the former fault study site to acquire higher resolution S-wave seismic and ground penetrating radar (GPR) data. The new seismic profiles show interruption of the reflectors in the stacked sections. Diffracted energy, changes in amplitude/shape of the reflection hyperbolae in the shot gathers and spatially coincident low velocity anomalies, also indicate the presence of several shallow fault strands deeper than 10 m. The GPR profile, overlapping and extending the seismic profiles in 30 m reaches a maximum investigation depth of about 15 m and shows the presence of deformation at three locations, one of which matches with one of the fault strands detected in the high-resolution S-wave seismic data. In this profile, sediment disruption was detected extending upwards to a depth as shallow as ca. 3.5 m, corresponding to alluvium with a poorly constrained age of ca. 2,300 yrs. Slip rate, maximum earthquake magnitude and recurrence, and other parameters are also estimated for the Porto Alto fault zone. These recently acquired seismic and GPR datasets indicate that there were at most three to five maximum earthquakes generated by the fault in the last 13,100 years, with an average recurrence of approximately 4,400 to 2,600 years respectively. However, the data show a grouping of these earthquakes in time, the first two in the period 13,100-12,300 years, separated by about 800 years, and the third or the last grouped three having occurred in the past 2,300 years with a similar average recurrence time of ca. 800 years. However, the regional historical and instrumental seismicity does not show an obvious link of any known major earthquake with the Porto Alto fault zone.

Keywords: Porto Alto fault zone, seismic hazard, seismic reflection, shear-waves, ground penetrating radar, fault parameters.

Resumo: A zona do Vale Inferior do Tejo (LTV), onde se situa Lisboa, foi afetada por vários sismos destrutivos de magnitude 6+, ainda por determinar. A identificação das roturas superficiais ou próximas da superfície esperadas para a região é uma tarefa desafiante que requer uma análise multidisciplinar que inclua técnicas geofísicas, uma vez que as zonas de falhas são maioritariamente cegas, apesar de provavelmente deformarem os depósitos aluvionares de idade plistocénica superior a holocénica do Rio Tejo. Este trabalho centra-se na caracterização da zona de falha de Porto Alto para fins de avaliação da perigosidade sísmica. A zona de falha de Porto Alto foi reconhecida nos dados de reflexão sísmica de ondas P da indústria petrolífera da década de 1980 como uma importante estrutura profunda do LTV reativada no Miocénico. Dados de reflexão sísmica de ondas P de alta resolução foram adquiridos posteriormente, no início dos anos 2000, para investigar atividade tectónica associada a esta estrutura no Holocénico, levando à identificação de algumas ramificações de falha pouco profundas, perto da superfície. No entanto, a resolução vertical destes perfis de reflexão sísmica de ondas P recém-adquiridos foi considerada insuficiente para corroborar qualquer rejeito vertical, presumivelmente pequeno, relacionado com rotura de falha nos cerca de 50 m de espessura das aluviões. Embora previamente testada na região de estudo, a metodologia de exposição da zona da falha através de trincheiras revelou-se uma tarefa difícil e pouco eficaz devido ao nível freático muito superficial (1 m) e à baixa coesão dos sedimentos. Neste trabalho revisitámos o local de investigação da zona de falha mais superficial para adquirir dados sísmicos de ondas S de alta resolução e de georadar (GPR). Os novos perfis sísmicos mostram interrupção de refletores nas secções sísmicas no domínio do tempo e em profundidade. A energia difratada, as alterações na amplitude/formato das hipérboles de reflexão nos registos de campo brutos, e as anomalias de baixa velocidade espacialmente coincidentes com as perturbações anteriores, indicam também a presença de várias ramificações de falha pouco profundas, localizadas a menos de 10 m de profundidade. O perfil GPR, sobrepondo-se aos perfis sísmicos adquiridos e prolongando-se 30 m para sul, atinge uma profundidade máxima de investigação de cerca de 15 m e indica a presença de deformação nas aluviões em três locais, um dos quais correspondente a uma das ramificações de falha detetadas nos dados sísmicos de alta resolução. No perfil GPR foi identificada uma rotura nos sedimentos que se estende para cima até muito próximo da superfície (cerca 3,5 m de profundidade), correspondendo a aluvião com uma idade mal constrangida de ca. 2300 anos. A taxa de deslizamento, a magnitude e recorrência do sismo máximo, e outros parâmetros, são também estimados para a zona de falha de Porto Alto. Os dados sísmicos e de GPR recentemente adquiridos apontam para três a cinco eventos máximos gerados pela falha nos últimos 13100 anos, com uma recorrência média de aproximadamente 4400 ou 2600 anos, respetivamente. Contudo, os dados evidenciam agrupamento

desses sismos no tempo, os dois primeiros no período 13100-12300, separados por cerca de 800 anos, e o terceiro, ou os três últimos agrupados ocorrendo nos últimos 2300 anos, com uma recorrência média semelhante, de ca. 800 anos. No entanto, a sismicidade histórica e instrumental regional não mostra uma ligação evidente de qualquer grande sismo conhecido com a zona de falha do Porto Alto.

Palavras-chave: Zona de falha de Porto Alto, perigosidade sísmica, refleção sísmica, ondas de corte, georadar, parâmetros de falha.

[1] Laboratório Nacional de Energia e Geologia, Apartado 7586 -Alfragide, 2610-999 Amadora, Portugal.
[2] Universidade de Lisboa, Faculdade de Ciências, Instituto Dom Luiz, Lisboa, Portugal.
[3] Delft University of Technology, Department of Geoscience and Engineering, P.O. Box 5028, 2628 GA Delft, The Netherlands.
[4] Universidade de Évora, Largo dos Colegiais 2, 7004-516 Évora and Center for sci-tech Research in EArth sysTem and Energy – CREATE, - Largo dos Colegiais 2, 7004-516 Évora, Portugal.

* Corresponding author / Autor correspondente: joao.carvalho@lneg.pt

1. Introduction

This study focuses on the localization and characterization of the active Porto Alto fault zone (PAFZ) in the Lower Tagus Valley (LTV) as a contribution to the seismic hazard evaluation in this densely populated area, which comprises the city of Lisbon and surroundings. The LTV area is sited in the Lower Tagus Cenozoic Basin, a complex tectonic depression filled with Cenozoic sediments, located approximately 300 km north of the plate boundary zone between Africa (Nubia) and Eurasia (Fig. 1a).

The PAFZ has a poor geomorphic expression and displaces recent soft sediments in this intraplate region with low-tectonic strain. Regional fault slip-rates are low, of the order of 0.05-0.3 mm/yr (*e.g.*, Cabral, 1995; Cabral *et al.*, 2004; Carvalho *et al.*, 2006; Canora *et al.*, 2015). However, the region has been affected by several destructive local earthquakes as in 1344 (poorly characterized), 1531 and 1909, which caused major loss of lives, and significant damages with major economic impacts (*e.g.*, Mendes-Victor *et al.*, 1994; Justo and Salwa, 1998; Ferrão *et al.*, 2016; Matos *et al.*, 2018) (Fig. 1b). The tectonic sources of these events have been attributed to local fault zones based on macroseismic descriptions and seismic intensity distribution data, and modelling of a Tagus estuary tsunami (*e.g.*, Baptista *et al.*, 2004). Nonetheless, the exact location of these active fault sources remains to be determined. The low slip-rates and the significant erosion/sedimentation rates make the identification of recent fault surface ruptures a difficult task, added to the fact that faults strands are buried beneath/within the Holocene alluvial cover. The instrumental seismicity, on the other hand, lacks in quality to refine the fault structures, particularly before the installation of the present-day seismic network around the year 2000 (*e.g.*, Custódio *et al.*, 2015, Fig. 1b). More recent seismic activity fails to show in the LTV a clear relationship with known active faults.

Therefore, the primary approach in the last two decades has been the use of geophysical techniques to investigate the subsurface, providing data for seismic hazard evaluation purposes (*e.g.*, Cabral *et al.*, 2003, Vilanova and Fonseca, 2004; Carvalho *et al.*, 2006, 2008). Oil-industry seismic reflection profiles, which cover a good part of the study area, have been used in the past to identify major fault zones at depth and to characterize the regional tectonic framework. However, these seismic data have a vertical resolution of 3-5 m in the shallowest hundreds of meters and are thus unsuitable to characterize shallow faults affecting recent soft sediments, where expected vertical fault offsets are in the range of 1 m.

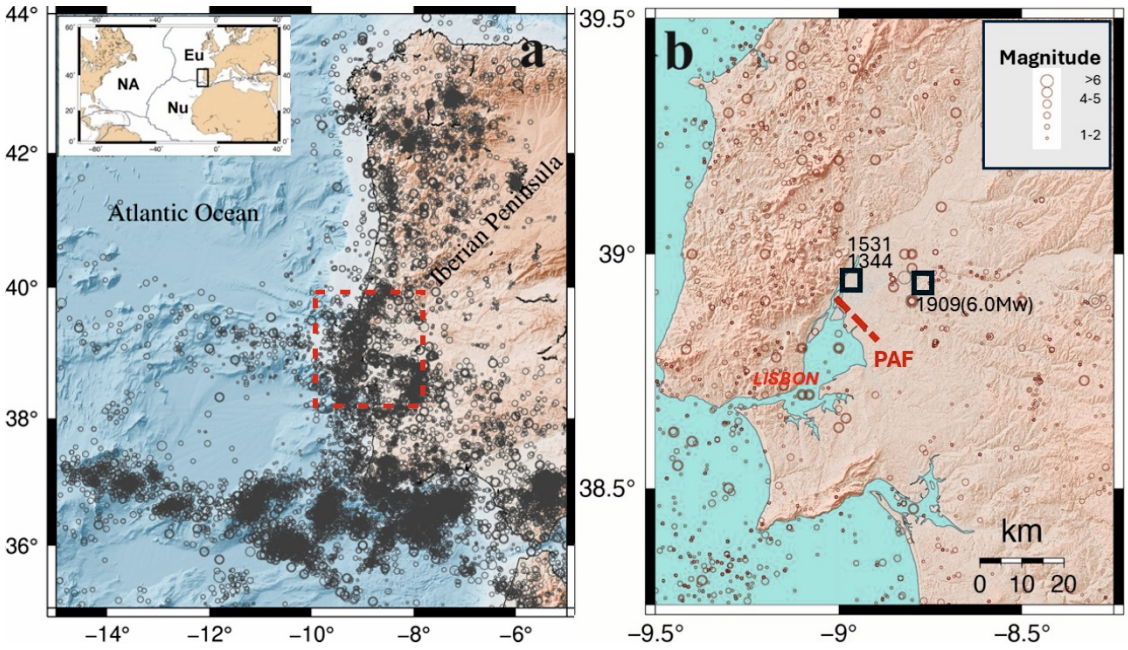

Figure 1. (a) Seismicity of mainland Portugal and adjacent area (65 BC to 2007, after Instituto Português do Mar e da Atmosfera - IPMA) and inset showing the regional tectonic setting; dashed square indicates location of the map shown in (b); Nu, Nubian Plate; Eu, Eurasian Plate; NA, North America Plate. (b) Zoom of figure 1a with location of the Porto Alto fault zone (PAF) and the local historical earthquakes.

Figura 1. (a) Sismicidade de Portugal continental e área adjacente (65 a.C. a 2007, segundo o Instituto Português do Mar e da Atmosfera - IPMA) e *inset* mostrando o enquadramento tectónico regional; o quadrado a tracejado indica a localização do mapa apresentado em (b); Nu, Placa Núbia; Eu, Placa da Eurásia; NA, Placa Norte-Americana. (b) Ampliação da figura 1a com localização da zona de falha de Porto Alto (FPA) e sismos históricos locais.

This is due not only to data resolution but also to an acquisition geometry that primarily focused on deeper targets. Therefore, research on shallow structures has been supported by shallow, high resolution geophysical data acquisition over selected target locations extrapolated from the oil industry profiles (*e.g.*, Carvalho *et al.*, 2006, 2009, 2016; Cabral *et al.*, 2013; Ghose *et al.*, 2013, 2023).

The analysis of several of the seismic profiles acquired for oil exploration in the Tagus River estuary supported an interpretation that WNW-ESE to NW-SE trending faults partially control the structural architecture of the Lower Tagus Cenozoic Basin in this area, which is also suggested by gravimetric data (Rasmunsen *et al.*, 1998; Cabral *et al.*, 2003; Carvalho *et al.*, 2006, 2017). This important structural direction is transversal to the main NNE-SSW / N-S trend in the Tagus Basin and is probably inherited from a transfer fault pattern linking the master NNE-SSW / N-S faults during the former Mesozoic extensional tectonics in West Iberia (ibid.).

The Porto Alto fault zone is one of the most significant transversal structures in the LTV Basin, which was recognized in two subparallel, ca. 6 km distant seismic lines (T16 and T14.4, figure 2, and fault 7 of figure 9 of Carvalho *et al.*, 2017), approximately between Alverca and Pancas, south of Porto Alto (Samora Correia, see locations in figure 2). This interpreted structure is a WNW-ESE trending, southerly dipping fault with apparent normal kinematics, limiting to the NE a cenozoic depocentre where sediments reach a maximum thickness of about 1,750 ms two-way-time (twt) (which corresponds roughly to 2,200 m, assuming a P-wave velocity of 2.5 km/s) south of the fault (Carvalho *et al.*, 2017). Subsidence affects the entire sedimentary column, although a main phase of activity is recognized in the interval corresponding to the lower half of the Cenozoic sediments (Cabral *et al.*, 2003; Carvalho *et al.*, 2006).

The Porto Alto fault zone is, therefore, a regional, WNW-ESE striking structure (Figs. 1b and 2) evidencing Cenozoic tectonic activity with a large dip-slip component, as found in the oil industry seismic data (Rasmunsen *et al.*, 1998; Cabral *et al.*, 2003; Carvalho *et al.*, 2006), although the fault zone is buried under Holocene alluvial sediments of the Tagus River, laying underneath a flat topography. This fault zone, recognized on oil industry seismic lines T14.4 and T16 (Fig. 2), was inferred as a ca. 10 km long structure linking the southern extension of the NNE-SSW Vila Franca de Xira fault to the northern extension of the N-S Pinhal Novo fault, at the NW and SE respectively (Cabral *et al.*, 2003; figure 3 of Carvalho *et al.*, 2006) (Fig. 2).

As the upper 50 to 60 m of the sedimentary cover corresponding to the Upper Pleistocene to Holocene alluvium (Vis *et al.*, 2008; Vis and Kasse, 2009) are poorly imaged in the oil-industry data, a site for acquiring high-resolution P-wave seismic reflection and vertical electrical soundings data was chosen based on the interpreted location of the Porto Alto fault zone at depth on the oil-industry T16 seismic line, ca. 9.5 km SW of Porto Alto (Samora Correia) (Figs. 2 and 3) (Carvalho *et al.*, 2006).

Figure 3 shows the stacked section of a reprocessed version of the P-wave seismic reflection profile T16 (Carvalho, 2004) with the location of the interpreted Porto Alto fault zone, while figure 4 shows the detailed arrangement of the previously acquired shallow P-wave profiles and vertical electrical soundings (VES) in the study site (Carvalho *et al.*, 2006). However, the 2-3 m of vertical resolution obtained in the alluvial sediments was still insufficient to investigate a fault with an assumed maximum 0.4 m of vertical offset inferred from a rupture length of 10 km and M_W 6.2 earthquake (based on Wells and Coppersmith, 1994, Cabral *et al.*, 2003; Carvalho *et al.*, 2006). Nevertheless, the shallow P-wave seismic reflection and VES data corroborated that the Porto Alto shallow fault zone corresponds to a deformation zone with several fault branches and suggested the presence of two branches reaching a relatively shallow depth, the northernmost approaching the surface to a depth of about 20 m (Carvalho *et al.*, 2006).

In this study, the former research site where P-wave seismic and VES data had been acquired (Carvalho *et al*., 2006) was revisited aiming to improve the quality of the previous observations through the acquisition of high-resolution S-wave seismic and ground penetrating radar (GPR) data. In fact, in the last few decades, the advantages of S-wave reflection data were recognized in multiple studies, and the method was proven as capable to map in detail shallow faulting (*e.g.* Goforth and Hayward, 1992; Ghose and Goudswaard, 2004; Pugin *et al.*, 2009; Harris, 2009; Ghose et al., 2013). The key advantages of S waves compared to P-waves at shallow depths are a higher resolution due to considerably low S-wave velocities in soft

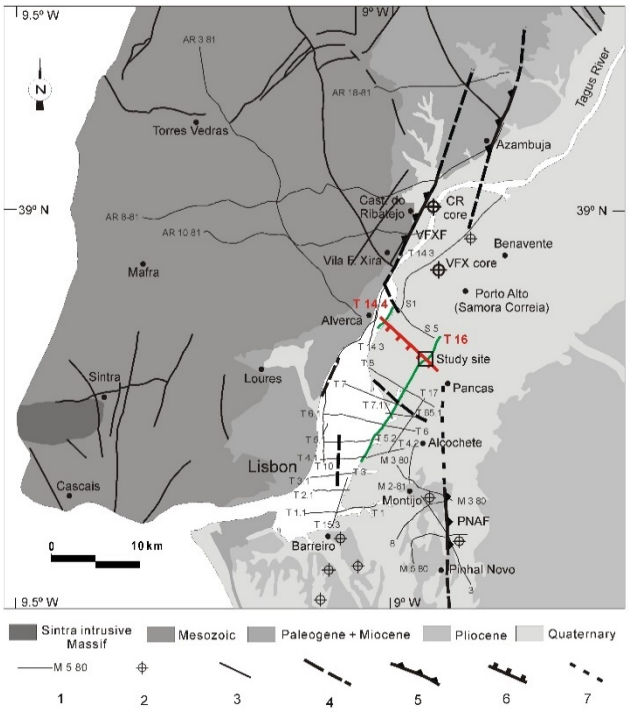

Figure 2. Simplified geological map of the LTV region, showing faults recognised on oil exploration seismic profiles (after Cabral *et al.*, 2003) and the location of the study site and the Porto Alto fault zone (in red). 1, seismic profile location; 2, oil exploration borehole; 3, previously mapped fault (I.G.M., 1992); 4, fault recognised on seismic section (certain and probable); 5, reverse fault; 6, normal fault; 7, presumed fault trace; PNAF, Pinhal Novo – Alcochete fault; VFXF, Vila Franca de Xira fault; CR core, Castanheira do Ribatejo core; VFX core, Vila Franca de Xira core; in green, seismic lines referred to in the text.

Figura 2. Mapa geológico simplificado da região do Vale Inferior do Tejo (LTV), mostrando falhas reconhecidas nos perfis sísmicos de pesquisa petrolífera (segundo Cabral *et al.*, 2003) e a localização do local de estudo e da zona de falha de Porto Alto (a vermelho). 1, localização de perfil sísmico; 2, furo de pesquisa de petróleo; 3, falha previamente mapeada (I.G.M., 1992); 4, falha reconhecida na secção sísmica (certa e provável); 5, falha inversa; 6, falha normal; 7, traço de falha inferido; PNAF, falha de Pinhal Novo – Alcochete; VFXF, falha de Vila Franca de Xira; CR core, sondagem de Castanheira do Ribatejo; VFX core, sondagem de Vila Franca de Xira; a verde, perfis sísmicos referidos no texto.

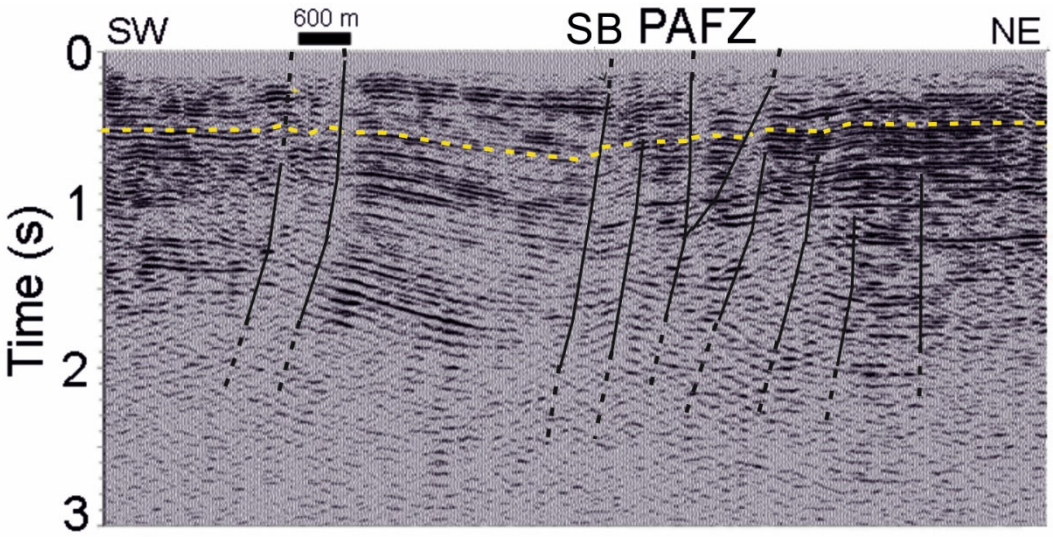

Figure 3. Revised interpretation of the northern sector of the earlier oil-industry seismic reflection profile T 16, where the Porto Alto fault zone was firstly identified by Cabral *et al.* (2003). PAFZ, Porto Alto fault zone; SB, shallow fault branch investigated in this work; dashed yellow line, base of Upper Miocene.

Figura 3. Interpretação revista do setor norte do perfil de reflexão sísmica da indústria petrolífera T 16, onde foi primeiramente identificada a zona de falha de Porto Alto (Cabral *et al*., 2003). PAFZ, zona de falha de Porto Alto; SB, ramificação de falha superficial investigado neste trabalho; linha amarela a tracejado, base do Miocénico Superior.

sediments, a higher sensitivity of S waves to subtle changes in the soft sediments (Ghose and Goudswaard, 2004), and also for being relatively insensitive to the presence of fluids. While a resolution of 2-3 m is expected for P-waves, based on previous data obtained at locations with a similar geological pattern as the present study site, for S-waves a resolution of approximately 0.4 m has been achieved in similar environments (*e.g.*, Ghose *et al*., 2013).

Figure 4 shows the location of the two S-wave reflection profiles (PA6 and PA7) and the GPR (PA8) profile used in this study. The GPR profile was acquired over the PA7 S-wave profile extending the seismic by more than 20 m, using a 100 MHz antenna that imaged to a depth of about 15 m.

As mentioned earlier, all profiles are located on the alluvial plain where alluvium sediments of the Tagus River were deposited in the last 15-20 kyr (Carvalho *et al.*, 2006; Vis *et al.*, 2008; Vis and Kasse, 2009). These 50 to 60 m thick, soft sediments are water saturated with the water table being generally very shallow, which favours the use of S waves, although the use of GPR remains still challenging.

2. Data acquisition and processing

2.1 Shear wave data

The target structure of the present study is a shallow fault branch of the Porto Alto fault zone identified in the old profiles (see profiles in figures 8, 9 and 10 from Carvalho *et al.*, 2006, and location in figure 4 here). The S-wave and GPR data acquisition was designed to image this fault branch. Both datasets were acquired along a hard dirt, non-paved road crossing the flat alluvial plain. Walk-away noise tests were at first performed with a 0.5 m geophone spacing to optimize the acquisition parameters. Walk-away data were acquired with 1.0 m minimum source-receiver offset using 96 geophones. From the maximum frequency and the minimum velocity observed in the walk-away data, we optimized the geophone spacing for the final reflection profiling at 0.75 m to ensure no spatial aliasing in the data.

A wooden beam pressed with the wheels of a 1.5 ton vehicle and hitting the beam from the side served as the S-wave source. To reduce P-wave contamination we hit both ends of the wooden beam with a sledgehammer and then subtracted one dataset from the other. Nevertheless, some P-wave arrivals are still observed in the raw data. This is likely due to the relatively hard, dry top surface road condition and the soft sediments beneath. The wavefield due to each hammer impact was recorded for 1 s with a sampling rate of 0.1 ms. Five pairs of hammer blows (5 blows at each side of the wooden beam) were stacked at each source point (hereafter called shot point).

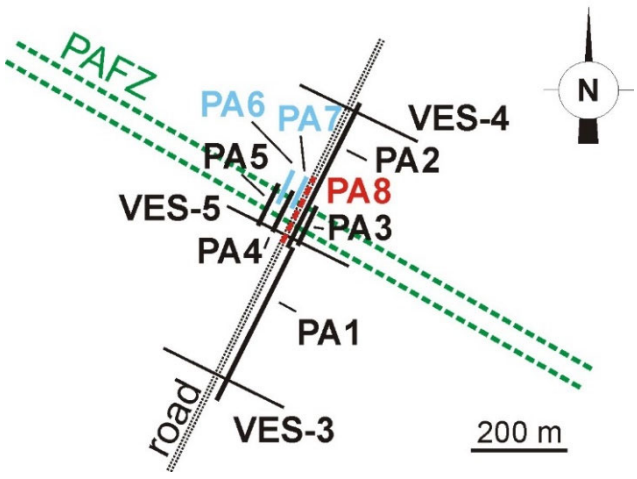

Figure 4. Location of previous shallow P-wave reflection profiles (PA) and vertical electrical sounding (VES) studies (in black), and S-wave reflection (cyan) and GPR (red) profiles investigated in this study; PAFZ – targeted shallow branch of the Porto Alto Fault Zone (in green).

Figura 4. Localização dos perfis superficiais de reflexão de ondas P (PA) e sondagens elétricas verticais (VES) realizados anteriormente (a preto), e perfis de reflexão de ondas S (a azul) e de GPR (a vermelho) efetuados neste estudo; PAFZ – traçado da ramificação superficial da Zona de Falha do Porto Alto investigada neste estudo (a verde).

With 48 active receiver channels spaced at 0.75 m in an inline, end-on geometry (source at the beginning of the receiver layout) and equally (0.75 m) spaced shots, we rolled-along every 12 channels/shots, that is, after 13 shot points, we moved the first 12 receivers (closest to the source) to the end of the receiver layout. By only processing the closest 36 receivers to the source we ensured a constant common-mid-point (CMP, Yilmaz, 1987) fold along the profile, allowing to minimize possible artefacts due to the uneven/varying stack fold and geometry, and thereby try to locate evidence of subtle faulting in the seismic reflection data. Therefore, in the data processing we used only 36 of the 48 active channels, achieving a nominal CMP fold of 18 along the stacked section. A minimum source-receiver distance of approximately 4.875 m was used. We also processed the data using full 48 channels and a split-spread geometry with varying fold along the profile, but the difference in quality of the stacked section was minimal.

Two parallel S-wave reflection profiles were acquired, the PA6 and the PA7 (Fig. 4). The PA6 profile was acquired over the alluvium while the PA7 was shot over a compacted landfill embankment built over the alluvium. We used commercial software (PGC, 2016) for processing both PA6 and PA7 profiles, following the sequence: geometry definition, vertical stacking (stacking the shot gathers for five pairs of hammer blows given at each source/shot point, to reduce the incoherent noise), trace editing, gain correction, bandpass filtering, first arrival muting, spectral whitening, velocity analysis, normal-moveout (NMO) correction, CMP stacking, surface consistent static corrections, revised velocity analysis and migration (Gazdag, 1978) (Figs. 5 and 6).

Migration moves reflectors up dip, collapses diffractions and improves resolution (*e.g*. Yilmaz, 1987). As the reflectors dips and diffractions in the stacked sections are minimal, migration did not produce additional benefits and migrated stacked sections are only shown in the supplemental material.

After performing velocity analysis and after calculating amplitude spectra of the stacked and shot gathers data, we estimated an average vertical resolution of ~0.3 m in the stacked sections, considering the vertical resolution = wavelength/4 Rayleigh criterion. Stacking velocities varied between 120 m/s and 180 m/s, while calculated spectrum showed a frequency content varying between 200 Hz, at shallow depths, and 80 Hz, at around 600 ms twt. Using the above-mentioned criterion, we have a maximum and minimum vertical resolution of 0.19 m and 0.5 m, respectively.

To confirm that there is little P-wave contamination, we changed the polarity of a few records and added them to the correspondent records of the hammering on the opposite side, resulting in negligible differences observed. Therefore, we processed two sections using data from each hammering side. This allowed us to verify the presence of incoherent, random noise and reinforce the validity of the interpreted geological features. At the end, we changed the polarity of one of the sides and added the second, but the improvement on the stacked section was minimal.

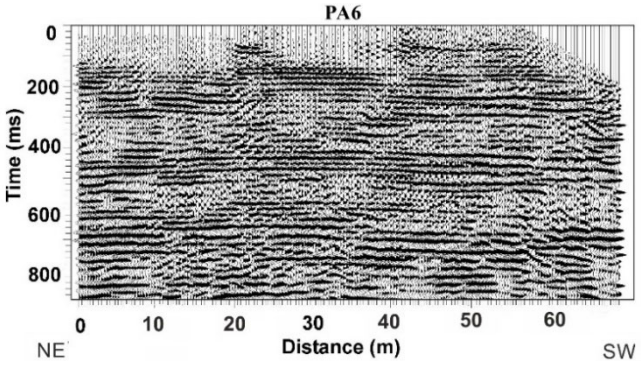

Figure 5. Post-stack migrated shear-wave seismic reflection profile PA6.

Figura 5. Perfil de reflexão sísmica de ondas S PA6 *post-stack* migrado.

Figures 5, 6, A1 and A2 highlight the high-quality of the time stacked sections and the repeatability of the seismic source, as well as the reproducibility of some specific structural features which will be discussed later. In the supplemental material (Fig. A3) the stacked sections for profile PA7 obtained by hammering the two sides of the wooden beam are shown. The similarity between these two sections is indicative of the fact that the prominent features observed in these sections are very likely to be geologically meaningful, and that they are not artefacts.

In the absence of vertical seismic profiles (VSP) or sonic log data, the time sections have been converted to depth using a representative 1-D interval velocity field obtained from the stacking velocity field and horizon velocity analysis (HOVA, see the next section). This reduces the possibility of introducing false discontinuities generated by laterally varying velocity fluctuations/errors. The results are shown in figures 5 and 6 for profiles PA6 and PA7.

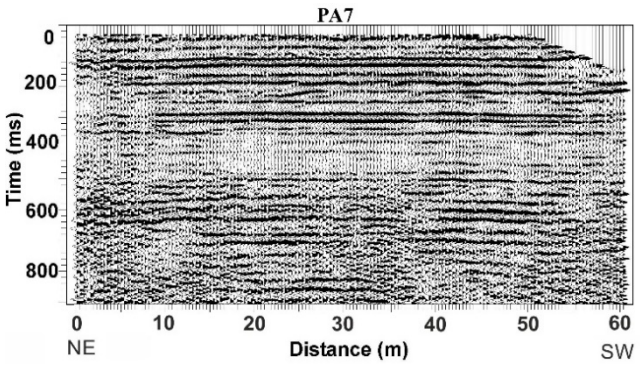

Figure 6. Post-stack migrated shear-wave seismic reflection profile PA7.

Figura 6. Perfil de reflexão sísmica de ondas S PA7 *post-stack* migrado.

2.2 GPR data

The ground penetration radar (GPR) profile was acquired along a single 95.2 m long line using a GSSI SIR-3000 acquisition system attached to a shielded antenna with a centre frequency of 100 MHz. The data were collected using a horizontal sampling of 50 traces per meter and a time window of 350 ns. The post-acquisition data processing (RADAN 6.6 - GSSI - software was employed for post-processing) involved zero-time adjustment, band pass filtering between 20 and 200 MHz, horizontal trace to trace averaging (5 traces), and the application of automatic gain control (AGC). An average velocity of 0.1 m/ns was used for depth estimation. The processed GPR profile is shown in figure 7b together with parallel seismic profile PA7, both interpreted. The choice of velocity directly affects the accuracy of depth calculations in GPR data. A velocity of 0.1 m/ns corresponds to typical conditions for materials like dry sand, non-saturated soils, or

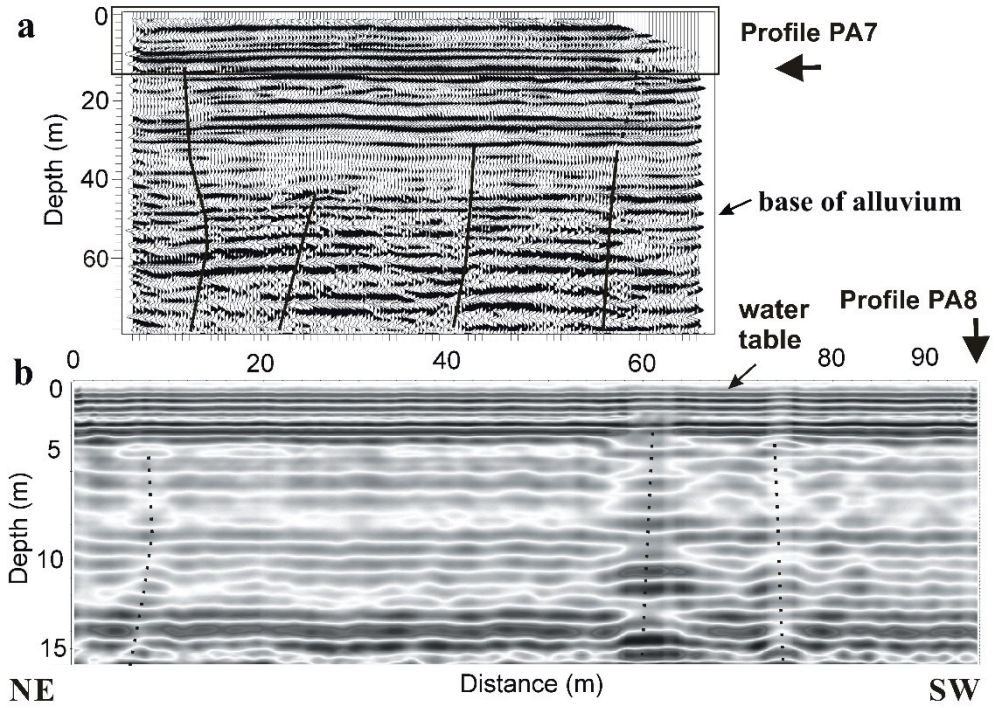

Figure 7. (a) Depth converted stacked shear wave section for profile PA7, using 1D average velocity from HOVA. The fault interpretation is superimposed. Rectangle indicates depth range of the GPR profile PA8 (see b). Base of the alluvium indicated by arrow interpreted from nearby boreholes. (b) GPR profile PA8. Dotted lines: possible fault strands/lithological changes.

Figura 7. (a) Perfil de ondas S PA7, *stacked* e convertido para profundidade utilizando a velocidade média 1D do HOVA. Interpretação de falhas sobreposta. O retângulo indica a profundidade alcançada pelo perfil GPR PA8 (ver b). Base da aluvião indicada pela seta interpretada a partir de sondagens próximas. (b) Perfil GPR PA8. Linhas ponteadas: possíveis falhas/variações litológicas.

clays. However, there is some uncertainty in these values due to the lack of calibration, as no ground-truth data (i.e., actual measurements in the field) are available to validate or adjust the assumed velocity.

3. Integrated data interpretation

Both stacked seismic sections (Figs. 5 and 6) show four major disruptions in the reflectors at distances from the origin of ca. 8 m, 19 m, 36 m and 52 m, showing coincident positions. This interpretation is shown in figure 7 for profile PA7, and in figure 10 for both profiles. Notice that the distance scale in figure 7 refers to the GPR profile (Fig. 7 b). In the GPR profile a few anomalies are also interpreted (Fig. 7). The northeastern one matches the fault strand that is observed in the seismic sections at location 8 m. The south-southwesternmost interpreted anomaly in the GPR profile is not sufficiently covered by the seismic data The anomaly located at around 61 m in the GPR profile, close to the end of the seismic sections, seems to match the southwesternmost fault strand interpreted in the seismic data. The two central fault strands observed in the seismic data are recognized to be deeper than the penetration of the GPR signal, as the penetration depth of the GPR is limited roughly to 15 m. The electromagnetic anomalies as detected in the GPR data do not show a clear vertical offset or disruption of the electromagnetic reflectors and may represent lithological changes. However, as these anomalies are well aligned along the vertical, we assumed them to be produced by fault strands.

To confirm the interpretation in the seismic stacked profiles shown in figures 7 and 8, and following the approach first proposed by Ghose *et al.* (2013), we investigated further to search for multiple evidence of faulting in the stacked sections, in shot gathers, and in the velocity field. These evidences include aligned diffractions in the unmigrated stacked sections, back-scattered/diffracted energy and undulations/breaks in the reflection hyperbolae in the shot gathers, and locations of sharp velocity changes/drops along a reflector.

To detect sharp velocity changes/drops, we performed HOVA, that uses root-mean-square (RMS) velocities, for four selected seismic horizons of the stacked sections PA6 and PA7. Figure 8 shows the HOVA analysis for PA7, with all velocity sharp changes larger than 10 m/s marked by arrows. We can recognize that the sharp or pronounced velocity changes occur very close to the locations of the perturbations that we also interpreted as faults in the stacked sections. Other causes for velocity changes may be lithological changes or uninterpreted fault branches.

Next, we carefully examined all shot gathers for PA7 and searched for disturbances in the reflection hyperbolae at the same positions. A few shot gathers examples are shown in figure 9. It can be observed that at the approximate locations of the fault strands interpreted in the stacked sections and HOVA, disturbances in the reflection hyperbolae are visible (shown by arrows in figure 9). The undulations and interruptions or breaks of the hyperbolae are noticed at approximately locations 36 m and 52 m. After data processing and interpretation, we revisited the site to check if any surface feature could explain the disturbances observed in the stacked data and shot gathers. No visible irregularities were observed in the dirt-road, which was very flat and homogeneous.

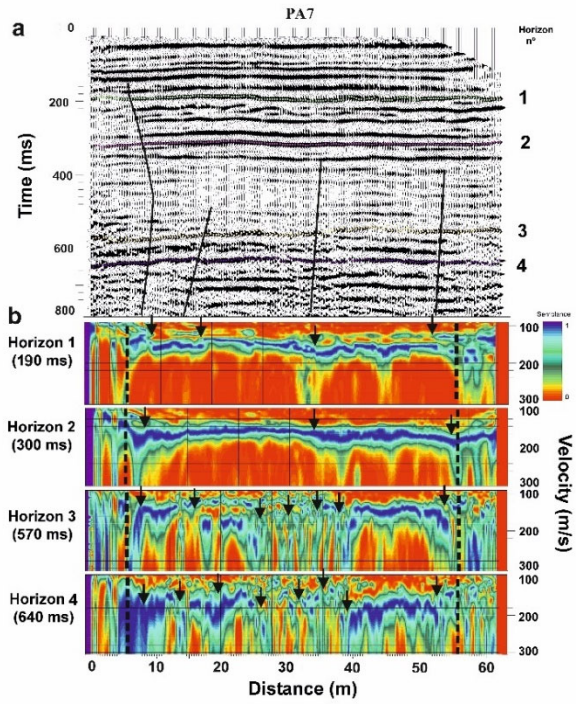

Figure 8. (a) Horizon velocity analysis (HOVA) for different seismic horizons indicated by numbers in the stacked section of profile PA7. (b) HOVA panels for distinct horizons; a time window of 70 ms was used in HOVA. Dashed lines indicate the end of central zone where the CMP fold is maximum and constant, and therefore the interpretation is more reliable. Arrows point to prominent velocity discontinuities. Note the coincidence of locations of most of the identified discontinuities with the location of the interpreted fault branches. Other locations may correspond to velocity changes caused by lithology or uninterpreted fault branches.

Figura 8 (a) Análise da velocidade de horizonte (HOVA) para diferentes horizontes sísmicos indicados por números na secção stack do perfil PA7. (b) Painéis HOVA para os distintos horizontes com uma janela temporal de 70 ms. As linhas a tracejado indicam os limites da zona central onde a cobertura sísmica (fold) é máxima e constante e, por isso, a interpretação é mais consistente. As setas apontam para descontinuidades de velocidade. Note-se a coincidência espacial da maioria delas com ramificações de falha interpretadas. Outras descontinuidades podem corresponder a mudanças de velocidade causadas pela litologia ou outras ramificações de falha não interpretadas.

The final interpretation taking into consideration the entirety of evidence in the seismic sections, shot gathers, velocity analysis, GPR and borehole data (Freitas *et al.,* 2018; Vis *et al*., 2008, 2016; Vis and Kasse, 2009) is presented over the seismic sections in figure 10. The stacked seismic sections were depth-converted using 1-D interval velocity field obtained from the RMS stacking velocity field previously mentioned, converted to interval velocities by the depth-conversion algorithm. The following interval velocities (time interval between brackets) were used: 155 m/s (0-200 ms), 175 m/s (200-360 ms), 185 m/s (360-435 ms), 195 m/s (435-580 ms), 246 m/s (580-1000 ms).

4. Discussion

The recognition and characterization of the recent tectonic activity of the PAFZ is important to improve knowledge of the seismic hazard in the Lower Tagus Valley region, particularly south of Vila Franca de Xira due to the fault location. As the fault zone is buried under several meters of Tagus River recent alluvia and evidence of deformation at the surface has not been identified, only a rough assessment of the fault length at the subsurface was made. It has been estimated to extend for approximately 10 km between the southern extension of the NNE-SSW trending Vila Franca de Xira fault (VFXF), at the NW, and the northern extension of the N-S trending Setúbal - Pinhal Novo - Alcochete fault (PNAF), at the SE, assuming that the Porto Alto fault zone works as a transfer fault linking those two major structures (Cabral *et al.*, 2003; Carvalho *et al.*, 2006) (Fig. 2).

Considering a thickness of ca. 25-30 km for the seismogenic layer (W_{seis}), inferred from the depth of the regional instrumental seismicity (Cabral *et al.*, 2013), and the relatively smaller fault length of approximately 10 km, we may assume an aspect ratio (L/W) of 1 for the maximum expectable earthquake fault rupture (*e.g.* Peruzza and Pace, 2002; Wesnousky, 2008) which corresponds to a rupture area of ca. 100 km^2. Taking these values as likely maximums and using empirical regressions between M_w and rupture length or rupture area proposed by different authors (Wells and Coppersmith, 1994; Stirling *et al.*, 2002), we estimated a moment magnitude of the maximum expectable earthquake that this fault may generate. Notice that these rupture parameters are poorly constrained and thus the estimated maximum earthquake should be considered with a high degree of uncertainty.

Due to the buried character of the studied fault, the inferred 10 km length was considered as a subsurface rupture length, corresponding to an expectable surface rupture of 75% of that value (7.5 km) (Wells and Coppersmith, 1994). Thus, both subsurface, and surface rupture length and M_w regressions of Wells and Coppersmith (*op. cit.*) were considered to estimate the magnitude of the maximum expectable earthquake. The regressions used refer to the normal slip type ("N") faults, considering the significant component of normal motion inferred for the studied fault, and to the "all" slip type faults, because of the higher statistical significance of the latter (Tab. 1).

Table 1. Regressions of fault rupture parameters and Mw, after Wells and Coppersmith (1994). RLD, subsurface rupture length; SRL, surface rupture length; RA, rupture area.

Tabela 1. Regressões entre parâmetros de rotura de falhas e Mw, segundo Wells e Coppersmith (1994). RLD, comprimento de rotura em profundidade; SRL, comprimento de rotura superficial; RA, área de rutura.

Regression	RLD / M_w	SRL / M_w	RA / M_w
	10 km	7.5 km	100 km^2
Mw=4.34+1.54 log (RLD) "N" Mw=4.38+1.49 log (RLD) "all"	5.58 ± 0.31 5.87 ± 0.26		
Mw=4.86+1.32 log (SRL) "N" Mw=5.08+1.16 log (SRL) "all"		6.01 ± 0.34 6.09 ± 0.28	
Mw=3.93+1.02 log (RA) "N" Mw=4.07+0.98 log (RA) "all"			4.95 ± 0.25 6.03 ± 0.24

Regressions developed by Stirling *et al.* (2002) were also used, although the 7.5 km surface rupture length assumed for the studied fault is slightly below the 10 km length lower bound of applicability of the length / magnitude regression proposed by those authors (Tab. 2).

Table 2. Regressions of fault rupture parameters and Mw, after Stirling *et al*. (2002). L, surface rupture length; A, rupture area.

Tabela 2. Regressões entre parâmetros de rotura de falhas e Mw, segundo Stirling *et al.* (2002). L, comprimento de rotura superficial; A, área de rotura.

Regression	L / M_w	A / M_w
	7.5 km	100 km^2
M_w=5.88+0.80 log (L)	6.58 ± 0.30	
M_w=5.09+0.73 log (A)		6.55 ± 0.26

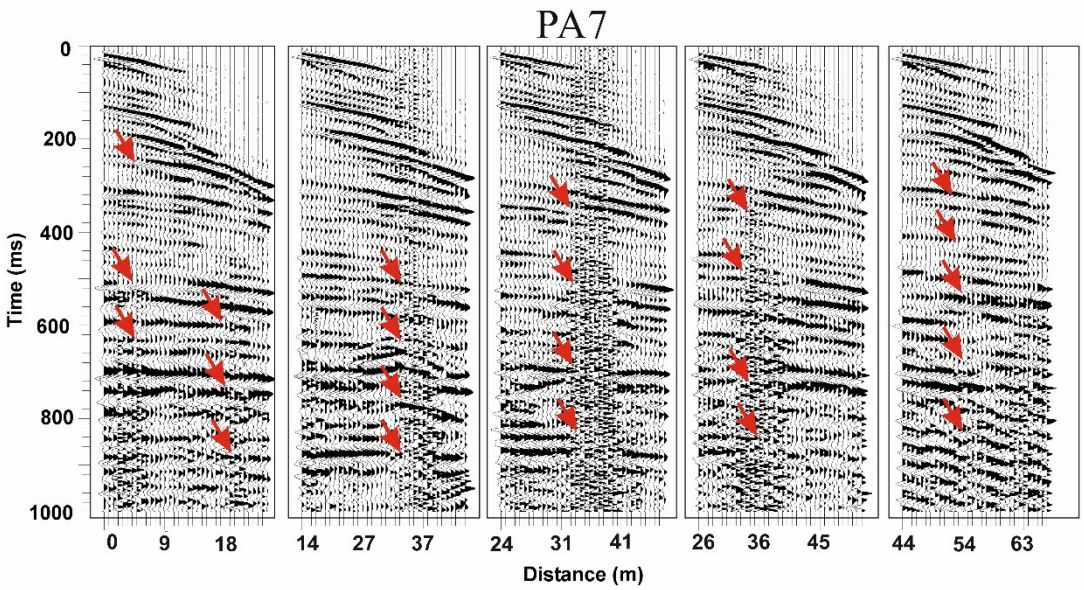

Figure 9. Examples of shot gathers from profile PA7 indicating breaks/undulations in the reflection hyperbolae at coincident locations (about 8 m, 19 m, 36 m, and 52 m), where interruptions in the stacked reflectors, diffractions and sharp velocity changes have been observed.

Figura 9. Exemplos de *shot gathers* do perfil PA7 indicando interrupções/perturbações das hipérboles de reflexão em locais coincidentes (cerca dos 8 m, 19 m, 36 m e 52 m), onde se observaram nas secções sísmicas as interrupções dos refletores, difrações e mudanças bruscas de velocidade.

We also estimated the coseismic displacement on the fault during the maximum expectable earthquake using empirical regressions of surface rupture length and maximum and average displacement, proposed by different authors (Wells and Coppersmith, 1994; Stirling *et al.*, 2002; Manighetti *et al.*, 2007) (Tab. 3).

As Stirling *et al.* (2002) suggest, the larger average surface displacement obtained using their "censored instrumental data" regression may be explained by the fact that it excludes all instrumental earthquakes with surface displacement less than 1 m and surface rupture length less than 5 km, and to a different scaling relationship for larger earthquakes compared to that of smaller earthquakes.

A fault-slip / fault length scaling law derived by Manighetti *et al.* (2007) based on the work of Shaw and Scholz (2001) proposes that for ruptures with $L \leq 2W_{seis}$ (where L is fault length and W_{seis} the thickness of the seismogenic layer), which is true in our case, $D_{max} = \alpha\ (L/2)$, where α depends on W, increasing with decreasing W_{seis}.

For a 25-30 km thick seismogenic layer, α should be valued between 21.5×10^{-5} and 50×10^{-5}, as derived by Manighetti *et al.* (*op. cit.*) for W_{seis} of 36 km and 18 km respectively. Accordingly, for a fault length L of 10 km, D_{max} for the studied fault should fall between the following values:

$D_{max} = 21.5 \times10^{-5}$ (10/2 km) = 1.1 m for W_{seis} = 36 km
$D_{max} = 50 \times10^{-5}$ (10/2 km) = 2.5 m for W_{seis} = 18 km

Taking an average surface displacement (D_{av}) = $D_{max}/2$ (Manighetti *et al.*, 2007), we estimate D_{av} to be valued between 0.6 and 1.3 m.

Considering all the regressions used, we may thus expect for the Porto Alto fault a D_{max} lying between ~0.2 and 2.5 m, and a D_{av} valued sbetween ~0.1 m and 1.7 m during the maximum expectable earthquake. The large variability of the inferred values reflects the high uncertainty in the estimates of the maximum and average coseismic displacement, with the lower bounds slightly smaller than the detection resolution of the seismic data (~0.3 m).

These estimates can be used to independently infer the magnitude range of the maximum earthquake by calculating the seismic moment, M_o, and the corresponding M_w, assuming an average rigidity $\mu = 3 \times 10^{10}$ Nm^2 for the crust (Tab. 4), which is consistent with the estimates given in table 1 and 2.

The vertical offset produced by the fault in the alluvial sediments will depend on fault dip and the rake of the slip line. Considering the high dip of the fault inferred from the seismic reflection evidence and the probable predominant (normal) dip-slip component inferred from the fault orientation in the regional tectonic framework, we may assume that the calculated maximum and average coseismic displacements are close to the coseismic vertical offsets produced by the fault ruptures on the alluvial sediments.

As the average vertical resolution of the newly acquired seismic profiles is approximately 0.35 m and considering most of the inferred estimates of the expected maximum and average coseismic

Table 3. Regressions of surface rupture length L (7.5 km) and coseismic displacement, after (a) Wells and Coppersmith (1994) and (b) Stirling *et al.* (2002) - (i) all instrumental earthquakes (N 95), (ii) censored instrumental earthquakes (N 50).

Tabela 3. Regressões entre o comprimento de rotura superficial L (7,5 km) e o deslocamento cossísmico, segundo (a) Wells e Coppersmith (1994) e (b) Stirling *et al.* (2002) - (i) todos os sismos instrumentais (N 95), (ii) sismos instrumentais censurados (N 50).

Regression	Maximum Displacement (D_{max}) (m)	Average Displacement (Dav) (m)
(a) log (D_{max}) = -1.38+1.02 log (L) "all" (a) log (D_{max}) = -1.98+1.51 log (L) "N"	0.33 + 0.54 / - 0.20) 0.22 + 0.34 / - 0.13)	
(a) log (D_{av}) = -1.43+0.88 log (L) "all" (a) log (D_{av}) = -1.99+1.24 log (L) "N"		0.22 + 0.28 / - 0.13) 0.12 + 0.17 / - 0.07)
(b) (i) log (D_{av}) = -0.81 + 0.56 log (L) (b) (ii) log (D_{av}) = 0.06 + 0.18 log (L)		0.48 (+ 1.00 / - 0.23) 1.7 (+ 1.22 / - 0.70)

Table 4. Maximum magnitude estimates from the seismic moment, assuming $\mu = 3\times10^{10}$ Nm^{-2}.

Tabela 4. Estimativas de magnitude máxima a partir do momento sísmico, assumindo $\mu = 3\times10^{10}$ Nm^{-2}

Rupture area A (km^2)	Average displacement D_{av} (m)	$M_o = D_{av}\times A\times\mu$ (Nm)	M_w
100	0.12	3.60×10^{17}	5.6
100	1.70	5.10×10^{18}	6.4

slip, we conclude that, although insufficient to accurately resolve single event vertical displacements, they provide a reasonable capacity for detecting expected maximum earthquake surface or near surface ruptures produced by the study fault, and thus to constrain its recent tectonic activity. The vertical resolution of ~0.25 m of the GPR profile further enhances the ability to detect ruptures affecting the younger, top 15 m of alluvium.

5. Seismogenic implications for the Porto Alto fault zone

As indicated in section 3, the interpretation of the seismic and the GPR profiles shows that the Porto Alto fault is represented by a fault zone comprising several branches spreading along a band ca. 50-60 m wide in the shallower sediments which include approximately 50 m of alluvium at the top.

Three of the fault branches (two detected in the seismic profiles and in the GPR profile, and a third one the GPR profile beyond the SW end of the seismic profiles) extend upwards to a depth of ~10 m as evidenced in the seismic data, ascending further to ≤ ~3.5 m, as shown in the GPR data (Fig. 7). Interference of the very shallow water table generates reverberations in the GPR profile that prevent the monitoring of the alluvium above this depth. These data suggest that three near surface fault ruptures affected the alluvial sediments presently at a depth of 3.5 m or even less.

Two other fault branches were recognized affecting the alluvium in the PA6 and PA7 seismic profiles that do not reach the upper sedimentary levels (Fig. 10). Using the PA7 profile as reference, we infer that these two fault branches extend upwards in the alluvium to depths of approximately 46 m and 32 m respectively (Figs. 7 and 10). Profile PA7 was considered as the reference because of its better data quality as it was acquired over a compacted dirt road built on the alluvium. This resulted in a velocity inversion at the surface (a high velocity top layer lying over a low velocity substrate) that reduced the interfering Love waves, thus improving finally the quality final of the image. The surface roughness/irregularity caused by a dry alluvium was also less for the compacted topsoil at this site).

The age of the alluvial sediments crossed by the seismic and the GPR profiles was estimated using data from the 52 m deep Vila Franca de Xira borehole (VFX core) referred in Vis *et al*. (2008) and Vis and Kasse (2009), which was drilled ~10 km NNE (upstream) of the Porto Alto seismic lines, as well as data from another borehole drilled approximately 5.5 km further N, located E of Castanheira do Ribatejo (CR core), which reached a depth of 46 m below m.s.l. (Freitas *et al*., 2018) (Fig. 2). Five radiocarbon dates were obtained in the VFX core at different depths (relative to the alluvial plain), two in the upper section, at -13 m (4090-3850 yrs cal BP) and -22 m (7270-7010 yrs cal BP) and the other three at -29 m (10200-9780 yrs cal BP), -37 m (11800-11200 yrs cal BP) and -49 m (14260-13780 yrs cal BP). In the CR core, three radiocarbon dates were obtained at depths (relative to m.s.l.; alluvial plain is ca. 2 m above) of -8 m (6571-6435 yrs cal BP), -17 m (9531-9406 yrs cal BP) and -30.5 m (14120-13809 yrs cal BP).

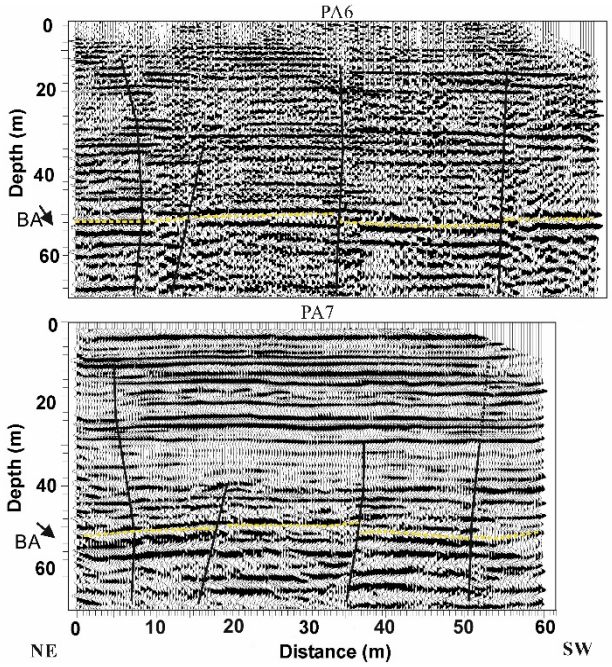

Figure 10. Final fault and stratigraphic interpretation for profiles PA6 (top) and PA7 (bottom) for depth-converted seismic stacked sections. BA: base of alluvium.

Figura 10. Interpretação final, estratigráfica e de falhas, para os perfis sísmicos PA6 (imagem superior) e PA7 (imagem inferior) convertidos para profundidade. BA: base das aluviões.

The age of the shallower sample of the VFX borehole core, at 13 m below the alluvial plain, corresponds to an average sedimentation rate of ca. 3.0 mm/yr, while the age of the shallower sample of the CR core, at 10 m below the alluvial plain, corresponds to an average sedimentation rate of ca. 1.5 mm/yr, which is half the value obtained for the VFX core suggesting a reduction of the sedimentation rate for the upper section of the alluvium sedimentary column. Using the later sedimentary rate as a reference, we may estimate the age of the alluvial sediments at the depth of 3.5 m, thus obtaining an age of ca. 2300 yrs for the uppermost disturbed alluvium evidenced in the GPR profile.

The same procedure applies to the alluvium at depths of 32 m and 46 m. For the depth of 32 m and using an average sedimentation rate of 2.6 mm/yr obtained from the dated samples at the depths of 29 m in the VFX core and 32.5 m in the CR core, we infer an age of ca. 12300 yrs, while for the depth of 46 m and using a sedimentation rate of 3.5 mm/yr obtained from the sample at -49 m depth in the VFX core, we infer an age of ca. 13100 yrs.

Considering these estimates and the data provided by the seismic and GPR profiles, we may infer that the last fault ruptures propagated upwards through three fault branches distributed along a strip approximately 60 m wide, affecting alluvium deposited about 2300 years ago or earlier. The later hypothesis of ruptures younger than 2300 yrs cannot be tested because the structural interpretation of the upper 3.5 m in the GPR profile is not reliable due to the interference of the shallow water table, as referred. The ruptures on the three shallow fault branches may correspond to a single seismic rupture event with the fault slip distributed over the three branches, or they may represent three distinct events.

Two other fault ruptures are recognizable in the seismic profiles. The older one affects the alluvium at a depth of 46 m, deposited ca. 13100 yrs ago. The other one affects the alluvium at a depth of 32 m, deposited ca. 12300 yrs ago. One possible

interpretation is that these fault ruptures occurred at different times and they correspond to two distinct seismic rupture events or, alternatively, they are related to a single seismic rupture event distributed across two fault branches reaching different levels, which occurred ca. 12300 yrs ago. Notice however that these fault ruptures may not have reached the coeval topographic surface, thus implying that the related earthquakes could be more recent.

The Porto Alto fault ruptures identified in the seismic and GPR profiles affecting the alluvial sediments of the Tagus River are expectedly related to M_w 5.6 to 6.6 maximum earthquakes that this active structure has the capacity of generating, as inferred in the previous chapter. Considering the hypothesis that they are related to three distinct seismic events, as commented above, we can infer an average earthquake recurrence time of ca. 4400 yrs in the last 13100 yrs, the last earthquake having occurred roughly 2300 yrs ago or earlier. Alternatively, if the three shallow fault branches detected in the GPR profile represent three distinct events, we infer five distinct earthquakes with an average recurrence time of ca. 2600 yrs. Notice, however, that the evidence points to an irregular pattern, the first two events being clustered in time, separated by ca. 800 yrs (13100-12300 yrs), the last three events occurring 10000 yrs later, clustered in the last 2300 yrs and with a similar average recurrence of ca. 800 yrs.

Slip rates of active faults in the Lower Tagus Basin are poorly constrained, with estimated values comprised between 0.05 and 0.3 mm/yr (*e.g.* Cabral, 1995; Cabral *et al.*, 2004; Carvalho *et al.*, 2006; Canora *et al.*, 2015). Considering these slip rates and the extreme values of the estimated coseismic D_{av} for the study fault (0.12 and 1.7 m) we may infer average return periods ($T = D_{av}/v$) for a maximum earthquake comprised between 34000 (1.7 m/0.05 mm/yr) and 400 yrs (0.12 m/0.3 mm/yr). This corresponds to a very wide time range, reflecting the high variability and the uncertainty in the slip rates and displacement values used.

The evidence that the last single or multiple earthquakes occurred approximately in the past 2300 yrs allows considering that they could be historical events. However, the historical earthquake registry in the Lower Tagus area is scarce and unreliable for the period before the 14th century (*e.g.* Custódio *et al.*, 2015). Even though there was a significant earthquake in the Lower Tagus Valley area circa 500 yrs ago (1531) (*e.g.*, Mendes-Victor *et al.*, 1994; Justo and Salwa, 1998; Ferrão *et al.*, 2016; Baptista *et al.*, 2014) the known historical seismicity does not indicate an obvious link to the Porto Alto fault zone for that event or for others.

6. Conclusions

We have consistently found changes in the amplitude/shape and phase of the reflection hyperbolae in the shot gathers of S-wave seismic data, as well as low-velocity anomalies, interruptions of the reflectors and phase changes in stacked sections at specific locations along the two S-wave seismic profiles, which we associate with fault strands affecting alluvial sediments as shallow as 10 m depth, reinforcing the evidence of the local presence of the Porto Alto fault zone and of its activity in the Holocene. The two shear-wave profiles show disturbances at similar locations to previously inferred fault strands based on shallow, high-resolution P-wave reflection surveys and vertical electric soundings data (Carvalho *et al.*, 2006). Shear wave data point to the presence of four fault strands, two of which are also suggested by GPR data pointing to a depth as shallow as 3.5 m. Considering the GPR data interpretation and the age estimated for the sediments at a depth of 3.5 m, we infer that the last single, or three earthquakes generated by the fault with surface or near surface rupture, occurred in the past ca. 2300 yrs. Two other fault ruptures, possibly related to two previous seismic events were also recognized in the seismic profiles, one having occurred ca. 12300 yrs and the other ca. 13100 yrs ago.

The geometry and size of the Porto Alto fault zone were re-evaluated and, using empirical regressions between M_w and fault surface rupture length or fault rupture area, we estimated a moment magnitude (M_w) of 5.6 to 6.6 for the maximum expectable earthquake. Maximum and average coseismic displacements were also estimated, with D_{max} lying between ~0.2 m and 2.5 m, and D_{av} lying between ~0.1 m and 1.7 m. Assuming these offsets, and a slip rate of 0.05 to 0.3 mm/yr as previously estimated for active faults in the Lower Tagus Basin, average return periods for the maximum earthquake lying between 34000 and 400 yrs were inferred, which correspond to an inconclusive long range of variation. The newly acquired seismic and GPR data point to an average earthquake recurrence time of ca. 4400 yrs in the last 13100 yrs, the last event having occurred roughly in the past 2300 yrs. Evidence though points to a clustering in time, with the first two events occurring in the period 13100-12300 yrs, separated by ca. 800 yrs, and the last single, or a set of last three events occurring 10000 yrs later, these clustered in the past 2300 yrs with a similar average recurrence of ca. 800 yrs. The regional historical seismicity however does not indicate an obvious link of known historical earthquakes to the Porto Alto fault zone.

Acknowledgements

This work was supported by Fundação para a Ciência e Tecnologia in the scope of Projects SISMOD/LISMOT (PTDC/CTE-GIN/82704/2006), ATESTA (PTDC-CTE/GIX 099548/2008) and NEFITAG (PTDC-CTE/GIX 099548/2008). We also acknowledge Bento Caldeira as PI of the ATESTA project. J. Borges acknowledges ICT – reference UIDB/04683/2020 (https://doi.org/10.54499/UIDB/04683/2020), and FCT – Fundação para a Ciência e Tecnologia, I.P., in the framework of the UIDB/06107 – Centro de Investigação em Ciência e Tecnologia para o Sistema Terra e Energia (CREATE). This work was also funded by FCT I.P./MCTES through national funds (PIDDAC) – UIDB/50019/2020 (https://doi.org/10.54499/UIDB/50019/2020), UIDP/50019/2020 (https://doi.org/1054499/UIDP/50019/2020) and LA/P/0068/2020 (https://doi.org/10.54499/LA/P/0068/2020). Dan Herold and Parallel Geoscience Corporation are acknowledged for providing an academic licence of Seismic Processing Software. The authors are grateful to the field crew: F. Caneiras, J. Leote, C. Cancela and J. Gomes. We are also grateful to Paula Figueiredo and Luís Matias for their comments and suggestions that significantly improved the manuscript.

References

Baptista, M., Miranda, J., Batlló, J., 2014. The 1531 Lisbon Earthquake: A Tsunami in the Tagus Estuary?. *Bulletin of the Seismological Society of America*, **104**: 2149-2161. https://doi.org/10.1785/0120130316.

Cabral, J., Moniz, C., Ribeiro, P., Terrinha, P., Matias, L., 2003. Analysis of seismic reflection data as a tool for the seismotectonic assessment of a low activity intraplate basin- the Lower Tagus Valley (Portugal). *Journal of Seismology*, **7**: 431-447. https://doi.org/10.1023/B:JOSE.0000005722.23106.8d.

Cabral, J., Moniz, C., Batló, J., Figueiredo, P., Carvalho, J., Matias, L., Teves-Costa, P., Dias, R., Simão, N., 2013. The 1909 Benavente (Portugal) earthquake: search for the source. *Natural Hazards*, **69**: 1211-1227. https://doi.org/10.1007/s11069-011-0062-8.

Canora, C., Vilanova, S. P., Besana-Ostman, G. M., Carvalho, J., Heleno, S., Fonseca, J., 2015. The Eastern Lower Tagus Valley Fault Zone in central Portugal: Active faulting in a low-deformation region within a

major river environment. *Tectonophysics*, **660**: 117–131. http://dx.doi.org/10.1016/j.tecto.2015.08.026.

Carvalho, J., Cabral, J., Gonçalves, R., Torres, L., Mendes-Victor, L., 2006. Geophysical Methods Applied to Fault Characterization and Earthquake Potential Assessment in the Lower Tagus Valley, Portugal. *Tectonophysics*, **418**: 277-297. https://doi.org/10.1016/j.tecto.2006.02.010.

Carvalho, J., 2004. *High-Resolution seismic applied to prospecting, geotechnical and seismic risk*. PhD thesis (in Portuguese), University of Lisbon, 250 (14 p. anexos).

Carvalho, J., Taha, R., Cabral, J., Carrilho, F., Miranda, M., 2008. Geophysical characterization of the Ota-Vila Franca de Xira-Lisbon-Sesimbra fault zone, Portugal. *Geophysical Journal International*, **174**: 567-584. https://doi.org/10.1111/j.1365-246X.2008.03791.x.

Carvalho, J., Ghose, R, Pinto, C., Borges, J., 2009. Characterization of a Concealed Fault Zone Using P and S-wave Seismic Reflection Data. *EAGE Near Surface*, **2009**: A14. 1-5. https://doi.org/10.3997/2214-4609.20146999.

Carvalho, J., Ghose, R., Alves, D., Leote, J., 2016, Earthquake faulting-related deformation in soil evidenced in S-wave shallow reflection data: field results from Portugal. *Geophysics*, **81**(5): IM97-IM108. https://doi:10.1190/geo2015-0040.1

Carvalho, J., Pinto, C., Rabeh, T., Dias, R., Torres, L., Borges, J., Torres, R., Duarte, H., 2017, Tectonic Evolution of an Intraplate Basin: The Lower Tagus Cenozoic Basin, Portugal. *Basin Research*, **29**(5): 636-557. https://doi.org/10.1111/bre.12193.

Custódio, S., Dias, N. A., Carrilho, F., Góngora, E., Rio, I., Marreiros, C., Morais, I., Alves, P., Matias, L., 2015. Earthquakes in western Iberia: improving the understanding of lithospheric deformation in a slowly deforming region. *Geophysical Journal International*, **203**: 127-145. https://doi.org/10.1093/gji/ggv285.

Ferrão, C., Bezzeghoud, M., Caldeira, B., Borges, J. F., 2016. The seismicity of Portugal and its adjacent Atlantic region from 1300 to 2014: Maximum Observed Intensity map (MOI). *Seismological Research Letter*, **87**(3): 743-750. https://doi.org/10.1785/0220150261.

Freitas, M. C., Cruces, A., Lopes, V., Cachão, M., Leira, M., Andrade, C., 2018. Realização de trabalhos geológicos para cumprimentos da Declaração de Impacte Ambiental do projecto "Cais Fluvial de Castanheira do Ribatejo". Final Report on the work by Instituto Dom Luiz (IDL), Faculty of Sciences, University of Lisbon, within the scope of the provision of services to the company CRIVARQUE, 35.

Gazdag, J., 1978. Wave-equation migration by phase shift. *Geophysics*, **43**: 1342-1351. https://doi.org/10.1190/1.1440899.

Ghose, R. Carvalho, J., Alves, D. V., Santos, L. A., Ressurreição, R., Alves, P. H. B., Leote, J., 2023. High-resolution P- and S-wave reflection studies of an intraplate structure: the Azambuja fault, Portugal. *Tectonophysics*, **859**: 229851. https://doi.org/10.1016/j.tecto.2023.229851.

Ghose, R., Carvalho, J., Loureiro, A., 2013. Signature of fault zone deformation in near-surface soil visible in shear-wave seismic reflections. *Geophysical Research Letters*, **40**: 1-5. https://doi.org/10.1002/grl.50241.

Ghose, R., Goudswaard, J. C. M., 2004. Integrating S-wave seismic reflection data and CPT using a multi-angle, multi-scale approach. *Geophysics*, **69**: 440-459. https://doi.org/10.1190/1.1707064.

Goforth, T., Hayward, C. 1992. Seismic reflection investigation of a bedrock surface buried under alluvium. *Geophysics*, **57**: 1217-1227. https://doi.org/10.1190/1.1443337.

Harris, J. B., 2009. Hammer-Impact SH-Wave Seismic Reflection Methods in Neotectonic Investigations: General Observations and Case Histories from the Mississippi Embayment, U.S.A.. *Journal of Earth Science*. **20**: 513-525. https://doi.org/10.1007/s12583-009-0043-y.

Justo, J., Salwa, C., 1998. The 1531 Lisbon earthquake. *Bulletin Seismological Society America*, **88**: 319-328. https://doi.org/10.1785/BSSA0880020319.

LNEG, 2010. Geological Map of Portugal scale 1: 1,000,000. National Laboratory for Energy and Geology.

Manighetti, I., Campillo, M., Bouleya, S., Cottona, F., 2007. Earthquake scaling, fault segmentation, and structural maturity. *Earth Planet. Sci. Lett.*, **253**: 429-438. http://dx.doi.org/10.1016/j.epsl.2006.11.004.

Matos, C., Custodio, S., Batllo, J., Zahradnik, J., Arroucau, P., Silveira, G., Heimann, S., 2018. An active seismic zone in intraplate west Iberia inferred from high-resolution geophysical data. *Journal of Geophysical Research: Solid Earth*, ***123***: 2885-2907. https://doi.org/10.1002/2017JB015114.

Mendes-Victor, L. A., Oliveira, C. S., Pais, I., Teves-Costa, P., 1994. Earthquake Damage Scenarios in Lisbon for Disaster Preparedness. *In*: Tucker, B. E., Erdik, M., Hwang, C. N. (Eds.), Issues in Urban Earthquake Risk. NATO ASI Series, *Springer*, **271**: 265-289. https://doi.org/10.1007/978-94-015-8338-1_18.

Parallel Geoscience Corporation, 2016. *SPW – Seismic Processing Workshop*, version 4.0, user's manual.

Peruzza, L., Pace, B., 2002. Sensitivity analysis for seismic source characteristics to probabilistic seismic hazard assessment in central Apennines (Abruzzo area). *Bollettino di Geofisica Teorica ed Applicata*, **43**(1-2): 79-100.

Pinto, C. C., 2011. Identification of Seismogenic Structures in the Lower Tagus Basin. MsC Thesis (in Portuguese), University of Évora, 128. http://repositorio.lneg.pt/handle/10400.9/1398.

Pugin, A., Pullan, S., Hubter, J., 2009. Multicomponent high-resolution seismic reflection profiling. *The Leading Edge*, **28**: 1248–1261. https://doi.org/10.1190/1.3249782.

Rasmussen, E. S., Lomholt, S., Andersen, C., Vejbæk, O. V., 1998. Aspects of the structural evolution of the Lusitanian Basin in Portugal and the shelf and slope area offshore Portugal. *Tectonophysics*, **300**: 199-225. https://doi.org/10.1016/S0040-1951(98)00241-8.

Shaw, B. E., Scholz, C. H., 2001. Slip-length scaling in large earthquakes: observations and theory and implications for earthquake physics. *Geophys. Res. Lett.,* **28**(15): 2995-2998. https://doi.org/10.1029/2000GL012762.

Stirling, M. W., Rhoades, D. A., Berryman, K., 2002. Comparison of earthquake scaling relations derived from data of the instrumental and preinstrumental era. *Bull. Seismol. Soc. Am.*, **92**: 812–830. https://doi.org/10.1785/0120000221.

Stirling, M., Goded, T, Berryman, K., Litchfield, N., 2013. Selection of Earthquake Scaling Relationships for Seismic-Hazard Analysis. *Bull. Seismol. Soc. Am.,* **103**: 2993-3011. https://doi.org/10.1785/0120130052.

Thorbecke, J., and D. Dragannov, 2011, Finite-difference modeling experiments for seismic interferometry. *Geophysics*, **76**: H1-H18. https://doi.org/10.1190/geo2010-0039.1.

Vilanova, S. P., Nemser, E., Besana-Ostman, G. M., Bezzeghoud, M., Borges, J. F., Brum da Silveira, A., Cabral, J., Carvalho, J., Cunha, P. P., Dias, R. P., Madeira, J., Lopes, F. C., Oliveira, C. S., Perea, H., García Mayordomo, J., Wong, I. Arvidsson, R., Fonseca J. F. D. B., 2014. Incorporating Descriptive Metadata into Seismic Source Zone Models for Seismic Hazard Assessment: A case study of the Azores-West Iberian region. *Bulletin of the Seismological Society of America*, **104**: 1212-1229. https://doi.org/10.1785/0120130210.

Vilanova, S. P., Fonseca, J. F. B. D., 2004. Seismic hazard impact of the Lower Tagus Valley Fault Zone (SW Iberia). *Journal of Seismology*, **8**: 331-345. https://doi.org/10.1023/B:JOSE.0000038457.01879.b0.

Vis, G.-J., Kasse, C., Vandenberghe, J., 2008. Late Pleistocene and Holocene palaeogeography of the Lower Tagus Valley (Portugal): effects of relative sea level, valley morphology and sediment supply. *Quaternary Science Reviews*, **27**: 1682-1709. https://doi.org/10.1016/j.quascirev.2008.07.003.

Vis, G.-J., Kasse, C., Kroon, D., Vandenberghe, J., Jung, S., Lebreiro, S. M., Rodrigues, T., 2016. Time-integrated 3D approach of late Quaternary sediment-depocenter migration in the Tagus depositional systems: From river valley to abyssal plain. *Earth Sci. Rev.,* 153: 192-211. https://doi.org/10.1016/j.earscirev.2015.11.002.

Vis, G.-J., Kasse, C., 2009. Late Quaternary valley-fill succession of the Lower Tagus Valley, Portugal. *Sedimentary Geology*, **221**: 19-39. https://doi.org/10.1016/j.sedgeo.2009.07.010.

Wells, D., Coppersmith, K., 1994. New empirical relationships among magnitude, rupture length, rupture width, rupture area, and surface displacement. *Bulletin of the Seismological Society of America*,84, 974–1002. https://doi.org/10.1785/BSSA0840040974.

Yilmaz, O., 1987. Seismic data processing (Investigations in Geophysics, Vol 2.). *Society of exploration Geophysics*, Tulsa, OK (USA), 526.

Supplementary material

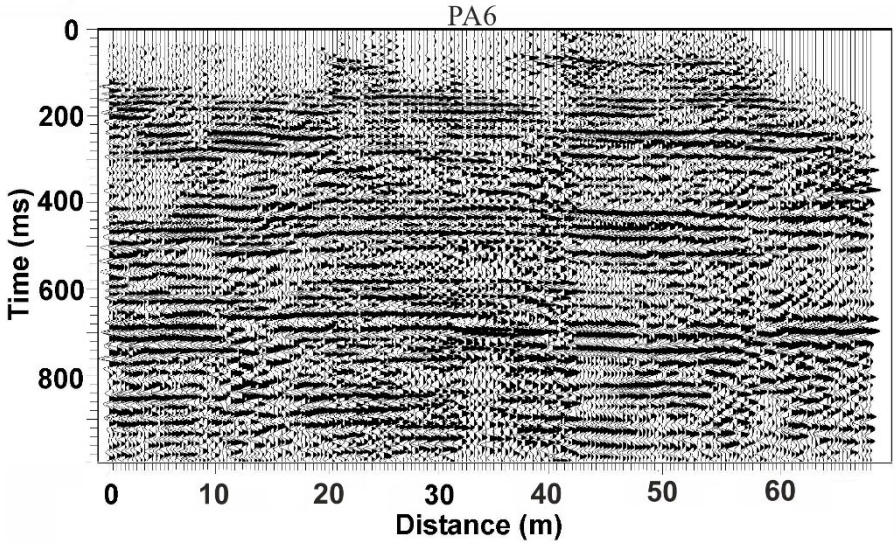

Figure A1. Processed, non-migrated shear-wave seismic reflection profile PA6.
Figura A1. Perfil de reflexão sísmica de ondas S PA6 processado, não migrado.

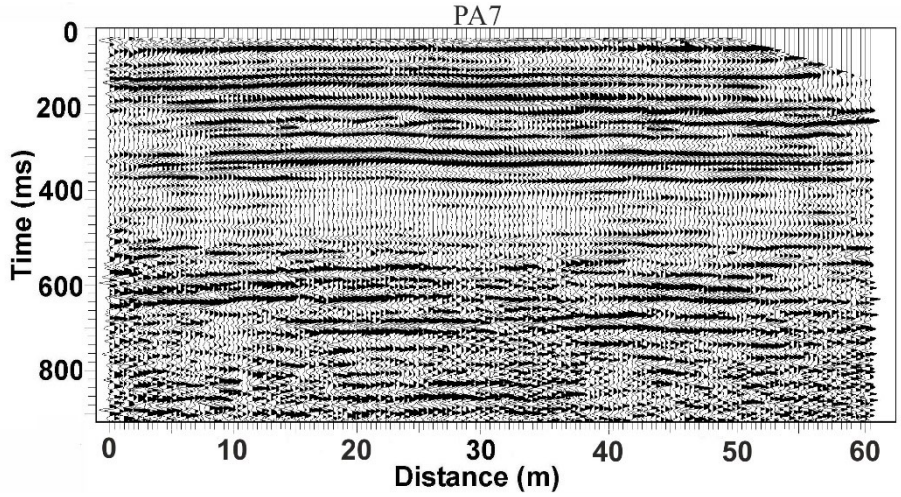

Figure A2. Processed, non-migrated shear-wave seismic reflection profile PA7.
Figura A2. Perfil de reflexão sísmica de ondas S PA7 processado, não migrado.

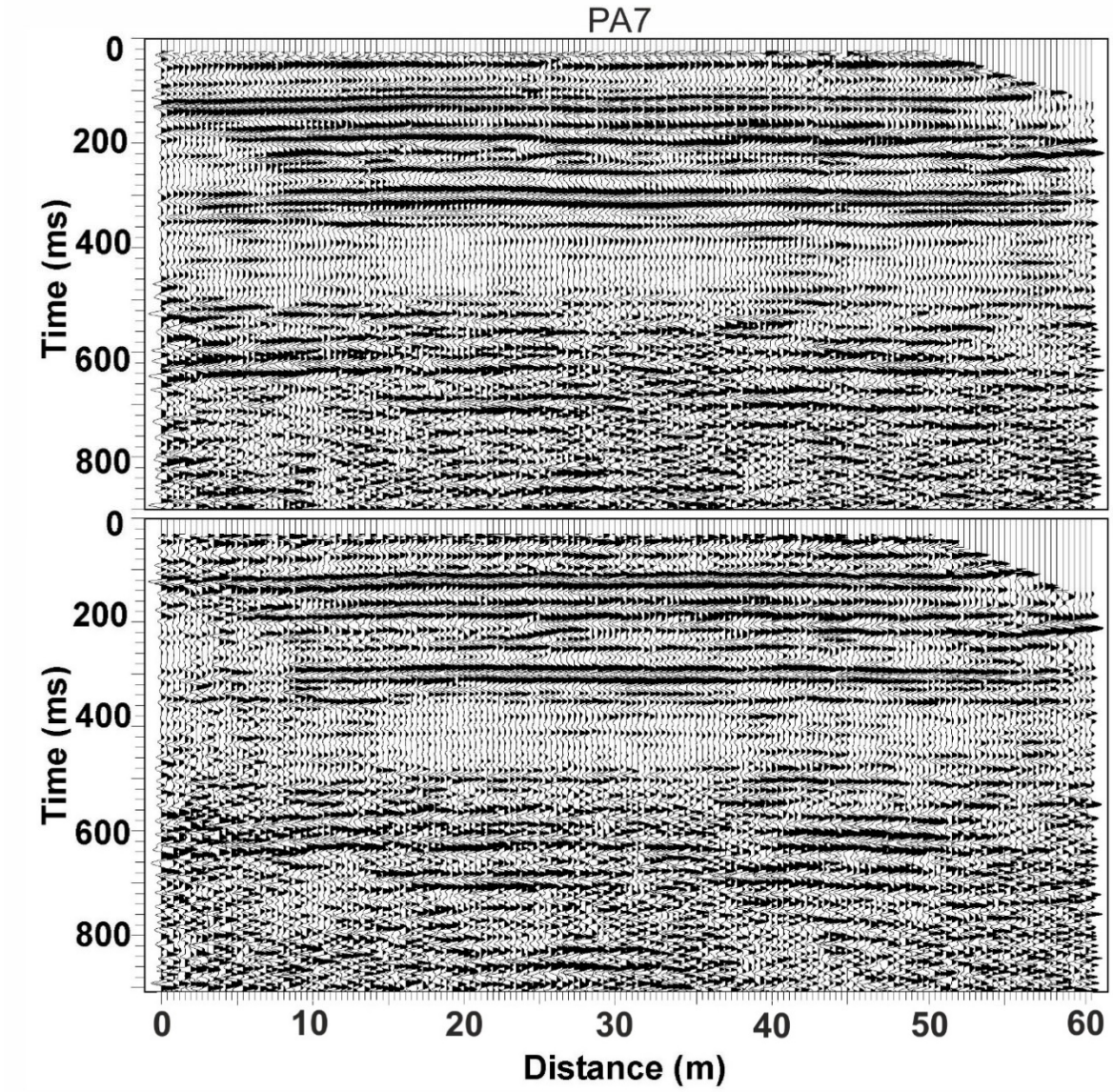

Figure A3. Shear-wave seismic reflection profile PA7 obtained with east (top) and west (bottom) hammer blows, demonstrating source repeatability.

Figura A3. Perfil de reflexão sísmica de Ondas S PA7 obtido com pancadas na fonte sísmica no lado este (topo) e no lado oeste (fundo), demonstrando a repetibilidade da fonte.